Ocean Modelling 191 (2024) 102421

Contents lists available at ScienceDirect

Ocean Modelling

journal homepage: www.elsevier.com/locate/ocemod

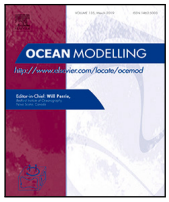

Estimation of Antarctic sea ice thickness through observation of wave attenuation

Francesca De Santi [a,b,*], Marcello Vichi [b,c], Alberto Alberello [d]

[a] National Research Council, Institute of Applied Mathematics and Information Technologies (IMATI-CNR), Milano, Italy
[b] Marine and Antarctic Research centre for Innovation and Sustainability (MARIS), University of Cape Town, Rondebosch, South Africa
[c] Department of Oceanography, University of Cape Town, Rondebosch, South Africa
[d] School of Engineering, Mathematics & Physics, University of East Anglia, Norwich, United Kingdom

ARTICLE INFO

Dataset link: https://data.mendeley.com/datasets/5b742jv7t5/1, https://doi.org/10.1594/PANGAEA.898400, https://doi.org/10.1594/PANGAEA.934732, https://cds.climate.copernicus.eu/cdsapp#!/dataset/reanalysis-era5-single-levels

Keywords:
Sea ice
Sea ice thickness
Marginal ice zone
Ocean waves
Southern ocean
PIPERS

ABSTRACT

The Close-Packing model – a physically based model for wave attenuation in sea ice – is used to infer sea ice thickness from wave observations collected in the Antarctic marginal ice zone during the PIPERS experiment. The model, calibrated for Arctic conditions, predicts ice thickness in good agreement with independent satellite measurements. The calibrated Close -Packing model, which is expressed in a simple monomial form, appears to have broad validity and, therefore, can be a suitable option for operational purposes.

1. Introduction

The marginal ice zone (MIZ) is the dynamic region of the ocean where sea ice transitions from open water to pack ice (Squire, 2022; Bennetts et al., 2022; Vichi, 2022). The interaction between surface gravity waves and the ice cover is a defining feature of the MIZ (Squire, 2022), and also plays an important role in its evolution (Boutin et al., 2020). Wave propagation in sea-ice contributes to ice breakup and melting, transfer of momentum between ice and ocean, and the mixing and stratification of the upper ocean (Iovino et al., 2022), whereas the presence of sea ice attenuates wave energy (Squire, 2020). For an enhanced representation of the ice–ocean system in climate models, it is therefore essential to model wave propagation in the marginal ice zone.

Over the last few decades, significant advances in modelling wave propagation in the MIZ have been supported by improved remote and in-situ measurements (Shen et al., 2018; Gebhardt et al., 2016; De Carolis et al., 2021; Thomson et al., 2018; Wadhams et al., 1988; Vichi et al., 2019; Kohout et al., 2020; Doble and Bidlot, 2013), as well as the development of numerical and theoretical approaches (Williams et al., 2017; Marquart et al., 2021; Keller, 1998; Herman, 2021; De Santi and Olla, 2017; Olla et al., 2021). However, a generally reliable modelling paradigm for wave attenuation in the MIZ has not yet been established, despite the known close relationship between sea ice properties and ocean waves (Bennetts et al., 2022).

Due to the continuous action of energetic Southern Ocean waves, large areas of the Antarctic MIZ (up to 5 million km^2) are composed of small floes in the form of frazil/grease/pancake ice (Wadhams et al., 1987; Alberello et al., 2019; Day et al., 2023). Widespread distribution of these ice types has recently been observed also in the western Arctic due to increased wave energy (Thomson et al., 2018). Since the length scales of floes are typically much smaller than ocean wavelengths, viscous-like dissipation dominates wave attenuation (Squire, 2020). This general framework, which leads to an exponential decay of the wave energy as a function of frequency, has been used extensively for decades (Wadhams et al., 1988; Keller, 1998; Meylan et al., 2018).

The exact mechanism assumed for energy dissipation results in the different parametrisation currently used in wave forecasting models (Rogers and Orzech, 2013). Parametric models typically describe the attenuation (rate) profiles, the set of attenuation rates k_i as a function of frequency f for a given point in space and time, as a

* Corresponding author at: National Research Council, Institute of Applied Mathematics and Information Technologies (IMATI-CNR), Milano, Italy.
E-mail address: francesca.desanti@cnr.it (F. De Santi).

https://doi.org/10.1016/j.ocemod.2024.102421
Received 15 April 2024; Received in revised form 26 July 2024; Accepted 12 August 2024
Available online 23 August 2024

power law increasing with frequency, $k_i = a_n f^n$. However, the available field campaign measurements of wave attenuation (Doble et al., 2015; Thomson et al., 2018; Montiel et al., 2022) show significant variations in the mean attenuation profiles and make it difficult to identify a single value for the power law exponent n (Rogers et al., 2021), and as result polynomial with no physical-basis have been used to calibrate the model for specific instances (Meylan et al., 2014, 2018). This implies some limitations of any simple parametric model that depends solely on frequency. Therefore, some ice properties, such as the thickness of the ice layer, need to be included in parametric models (Thomson, 2022; Yu et al., 2022; Doble et al., 2015; Wadhams et al., 2004).

Among the physical-based models, the so-called Close-Packing (CP) model (De Santi and Olla, 2017), i.e. an extension of the classical viscous layer model proposed by Keller (1998) that is more suited to pancake ice (Squire, 2020), can overcome the limitations. Dedicated analysis and comparison with field data (De Santi et al., 2018) have demonstrated that the attenuation rates predicted by the CP model can be expressed with a simple monomial power-law dependence on both frequency and ice thickness h, namely $k_i = Ah^{3/2}f^5$. A calibration procedure based on measurements in the Odden Ice Tongue in Greenland Pedersen and Coon (2004) provided an empirical estimate of the coefficient A (De Carolis et al., 2021) , which is related to the sea ice viscosity. The calibrated CP model was then validated with data from the Office of Naval Research (ONR) Departmental Research Initiative (DRI) "Sea State and Boundary Layer Physics in the Emerging Arctic Ocean" (Thomson et al., 2018) (hereafter referred to as Arctic Sea State). The results show remarkable agreement with in-situ observations (De Carolis et al., 2021) Collectively, the findings indicate that the estimated coefficient A is not site-specific, but may have a wider validity.

The present study investigates the application of the calibrated CP model in Antarctic sea ice. To achieve this goal, we test the model using the currently largest dataset of Southern Ocean MIZ wave measurements, collected during the 2017 Polynyas, Ice Production, and Seasonal Evolution in the Ross Sea (PIPERS) experiment (Kohout et al., 2020). Given a thickness dependent dispersion relation the sea ice thickness can be inferred from the wave attenuation profile (Wadhams et al., 2004). An Antarctic sea ice thickness product developed for thin ice conditions (Tian-Kunze and Kaleschke, 2021; Kaleschke et al., 2024) is used to assess the validity of sea ice thickness estimates with the calibrated CP model, and hence the validity of the model.

2. The calibrated close-packing model

The CP model (De Santi and Olla, 2017) is a generalisation of Keller's viscous layer model (Keller, 1998). This family of models treat sea ice as a continuous viscous and isotropic fluid of finite thickness and the underlying ocean as an inviscid fluid. Continuous mathematical models are physically appropriate in the MIZ, where sea ice floe sizes are much smaller than typical wavelengths; they also assume an homogeneous layer at 100% sea ice concentration, which is also realistic when considering a combination of pancake ice and grease ice in closed drift conditions (Vichi, 2022). For this reason, the CP model assumes a uniform layer of grease ice in which the ice floes are embedded and sufficiently close, i.e. close-packing, so that contact forces between them are non-negligible. The main advantage of the CP model compared to Keller's model is the ability to separate the contribution to the dynamics from the interstitial grease ice (or any other source of effective viscosity) from that of the sea ice floes.

The CP model simplifies the interaction between waves and floes by using a third imaginary layer at the interface between the grease ice and the atmosphere, where floes are ideally trapped. The surface motion of the wave can push the floes closer together and anelastic collisions can occur since the inertia of the floes is small. In this framework, the floes remain fixed in position relative to their neighbours and appear to the wave as horizontally rigid agglomerates whose extent scales with wavelength rather than individual floe size. The agglomerate, similarly to small plates tied into a regular lattice, allows flexibility in the normal direction but not in the tangential direction. The flexibility is lost when the length scale of the deformation, i.e. the wavelength, is comparable to the size of the floes. In this case, the CP model is no longer applicable. The detailed mathematical derivation can be found in De Santi and Olla (2017).

Wave models in sea ice are characterised by a dispersion relation linking the wave angular frequency ω , where $\omega = 2\pi f$, and the complex wave number $k = k_r + ik_i$, where the real part of the wave number defines the wave dispersion and the imaginary part the wave attenuation rate. The dispersion relation of the CP model can be approximated as:

$$k \simeq k_0 + \frac{\rho_i}{\rho_w}\left(k_0^2 h + \frac{i\sqrt{g}}{3}\frac{h^3}{\nu}k_0^{5/2}\right) \tag{1}$$

where $k_0 = \omega^2/g$ is the open water wave number, $g \simeq 9.81\ \mathrm{ms}^{-2}$ is the acceleration due to gravity, $\rho_i = 917\,\mathrm{kg\ m}^{-3}$ and $\rho_w = 1025\,\mathrm{kg\ m}^{-3}$ are sea ice and water density respectively, h and ν the sea ice layer thickness and effective viscosity.

The real part of the wave number in Eq. (1) agrees with the prediction of the mass loading model (Keller and Weitz, 1953) in the limit of ice thickness much smaller than the wavelength ($k_0 h \ll 1$). The mass loading model predicts a shortening of the wavelength due to the additional weight of the ice. Mainly due to the difficulty of making measurements, few field data are available for validation. Measurements from ship-borne X-band radars and Lagrangian wave buoys during the Arctic Sea State program are in agreement with the mass loading model (Collins et al., 2018).

Eq. (1) shows that the simultaneous estimation of ice viscosity and thickness values from attenuation data is an underdetermined problem (De Santi et al., 2018), common to all viscous-based models. In De Carolis et al. (2021) an empirical relationship between ice viscosity and thickness is used to close the problem. Based on dimensional analysis, it is assumed that $\nu = \eta g^{1/2} h^{3/2}$. A physical interpretation of thickness-dependent viscosity has been investigated in Olla et al. (2021). In De Carolis et al. (2021) the value of the unique free parameter η, has been determined by a calibration procedure performed with data from the 1997 Odden Ice Tongue (Pedersen and Coon, 2004), finding the value of η close to unity ($\eta = 0.963 \pm 0.093$). It is worth noting that this value of η results in an ice viscosity of $\nu \simeq 3h^{3/2}$, which aligns with laboratory measurements of grease ice (De Carolis et al., 2021).

The damping rate of the calibrated CP model therefore reads

$$k_i(\omega; h) = \frac{\rho_i}{\rho_w}\frac{1}{3\eta}h^{3/2}k_0^{5/2}. \tag{2}$$

For many oceanic applications it can be convenient to express Eq. (2) in terms of the frequency $f = \omega/(2\pi)$, which reads

$$k_i(f, h) = \frac{\rho_i}{\rho_w}\frac{1}{3\eta}\left(\frac{2\pi}{\sqrt{g}}\right)^5 h^{3/2}f^5 = Ah^{3/2}f^5 \tag{3}$$

with $A \simeq 10\ \mathrm{s}^5\ \mathrm{m}^{-5/2}$.

3. Data sources and processing

3.1. PIPERS attenuation profiles

The attenuation profiles were obtained from the wave measurements taken during the 2017 PIPERS cruise (Kohout et al., 2020). The attenuation profile $k_i(f)$ for each observed spectral energy density $E(f)$ was calculated by Rogers et al. (2021) using the state-of-the-art spectral wave model WAVEWATCH III (WWIII) (Tolman et al., 2009) by comparing the modelled energy density spectrum with the corresponding observed. Restricting the description of the WWIII equations to the needs of this study, the spectral energy density evolves as

$$\frac{DE}{dt} = \alpha(S_{\mathrm{in}} + S_{\mathrm{wc}} + S_{\mathrm{nl}}) + cS_{\mathrm{ice}_{1,2}}, \tag{4}$$

where D/dt denote the total derivative and c is the sea ice cover fraction. The source terms S are the energy inputs from wind (S_{in}), dissipation by whitecaps (S_{wc}), four-wave nonlinear interactions (S_{nl}), and sea ice dissipation ($S_{\text{ice}_{1,2}}$). The scaling of the open water source term α is an open question. Emmanuel et al. (2022). Therefore, two model data inversions are provided in Rogers (2020):

1. $\alpha = 1 - c$ the open water source terms are scaled by the open water fraction (the default in WWIII). All results related to this scaling are given here with the suffix 1.
2. $\alpha = 1$, open water source terms are not directly affected by ice cover. All results concerning this scaling are indicated hereafter with suffix 2.

Neither of these values is likely to be the most accurate, but they should represent the extremes of the set of effective scaling factors (Herman).

The source term package 4 (ST4; Ardhuin et al. (2010)) has been employed for S_{in} and S_{wc}, while the Discrete Interaction Approximation (DIA; Hasselmann and Hasselmann (1985)) has been used for S_{nl}. The sea ice dissipation term, which represents the unknown in Eq. (4), is then estimated and the attenuation profiles are obtained as

$$k_{i_{1,2}} = -\frac{S_{\text{ice}_{1,2}}}{(2c_g E)} \tag{5}$$

where c_g is the wave group velocity. For each choice of α, a total of 9477 attenuation profiles were obtained from 6 to 30 June 2017, divided into 16 frequency bins covering the frequency range 0.042 to 0.47 Hz (Rogers, 2020). Attenuation is not an instantaneous process but an integrated effect, encompassing the impact on the wave spectrum at up-wave locations. The resulting attenuation profiles should be interpreted as the total attenuation experienced by the wave from the point it enters the ice until it reaches the buoy.

To accurately analyse the attenuation rate, it is necessary to also consider the direction of the waves. As the PIPER dataset does not provide this information, we use the hourly mean wave direction from the fifth generation ECMWF reanalysis (ERA5), obtained from the Copernicus Climate Services (Hersbach et al., 2023).

3.2. Complementary sea ice data sets

Sea ice thickness (SIT) information for the PIPERS expedition comes from two sources: in-situ observations during deployment (Kohout et al., 2020) and remotely sensed data. The in-situ observations are only available at sampling sites, hence they cannot provide information on the conditions from the ice edge to the buoy.

Remote sensed data on SIT in Antarctica are difficult to obtain, mainly due to the difficulty of estimating snow cover on sea ice (Kurtz and Markus, 2012) and the limited validation data (Williams et al., 2015). Errors in current large-scale SIT estimates for Antarctica can reach around 50%, and basic statistical models of small-scale mean thickness also have high errors (Mei et al., 2019). An experimental version of the Antarctic SIT estimates from the Soil Moisture and Ocean Salinity (SMOS) mission, one of the European Space Agency's Earth Explorer missions, is publicly available (Tian-Kunze and Kaleschke, 2021). A method for inferring SIT from SMOS L-band microwave measurements of brightness temperatures previously developed for the Arctic has been adopted to the Antarctic with ad-hoc modified auxiliary data. The SMOS SIT product up to a thickness of about 1 m is delivered as daily averages and uncertainties on a polar stereographic projection grid with a resolution of 12.5 km (Kaleschke et al., 2024).

While the retrieval of SIT for the Antarctic has been improved with this new version (v3.3), the method is based on the assumption of a completely closed sea ice cover (100% sea ice concentration), which is often not met in the MIZ and results in a systematic underestimation of sea ice thickness. To evaluate the quality of SMOS estimates, the sea ice concentration (SIC) product is therefore required. Here we use as a reference the SIC obtained by the ARTIST Sea Ice (ASI) algorithm on microwave radiometer data from the Advanced Microwave Scanning Radiometer 2 (AMSR2) sensor of the JAXA GCOM-W1 satellite (Melsheimer and Spreen, 2019). SIC is provided as a daily average on a 6.25 km grid.

3.3. Processing workflow

The analysis was performed on the full data set according to the following processing steps.

- Define the ice edge for each day based on a sea ice concentration threshold of 15%. If SIC is less than 15%, consider it as open water.
- Calculate the hourly mean attenuation profile $k_i(f)$ and the mean position for each buoy to match the coarser temporal resolution of the tertiary data.
- Use the CP model described in Section 2 to infer sea ice thickness for each attenuation profile and both rescaling factors α

$$h_{\text{CP}_{1,2}} = \text{mean}_f \left(\frac{k_{i_{1,2}}(f)}{A\, f^5} \right)^{2/3} \tag{6}$$

- Determine the mean wave direction value θ nearest to the buoy located closest to the ice edge.
- Calculate the transect from the ice edge to the buoy location if the mean wave direction is towards the southern sector. Exclude the instance if waves originate from the pack ice and propagate towards northern sectors, i.e. for $\theta \in [90°, 270°]$.
- Compute the average SIT h_{SMOS} and the average SIC c for each transect to account for the average properties of the ice traversed by the wave before reaching the buoy.

Although there are potentially 5400 (25 days × 24 h × 9 buoys) attenuation profiles, only 2006 remains at the end of the processing workflow (some profiles in the original dataset were NaN and others were excluded for the mean wave direction).

Note that although the CP model is originally based on the assumption of high ice concentration, Eq. (6) can be extended to low concentration since the dissipation term, and hence $k_{i_{1,2}}$, has already been rescaled by the sea ice fraction. As discussed in Doble et al. (2015), $h_{\text{CP}_{1,2}}$ is an equivalent ice thickness which takes into account the thickness of both the grease ice layer and the thickness of the floes ($h_{\text{CP}_{1,2}} = (c_g h_g + c_f h_g)/c$, where the subscript 'g' denotes values related to grease ice, and 'f' refers to the ice floes). However, given the physical assumptions underlying the CP model, it is reasonable to assume that there is a threshold value of c below which this extension is no longer valid.

Fig. 1 shows maps of SIT and SIC, together with buoy positions and corresponding sea ice transects considered according to the methodology described above. The image refers to the 7th of June 2017, chosen as one of the few cases where the full nine buoys have a valid attenuation profile (Rogers, 2020).

4. Results

Fig. 2 compares the attenuation profiles obtained with the two rescaling of the open source terms for the configuration shown in Fig. 1. The attenuations k_{i_1} (with $\alpha = 1 - c$) are indicated by triangles and k_{i_2} (with $\alpha = 1$) are indicated by circles. The main differences between these two attenuations are observed at high frequency (short waves) for the buoys closer to the ice edge. This is where the wind input is expected to be significant. In these cases, the attenuation obtained by assuming the open water source terms unaffected by the presence of ice has higher values and is close to f^5, resulting in a better agreement with the CP predictions (shown in grey in Fig. 2). This trend is further validated by analysing the complete data set. Specifically, the best fit

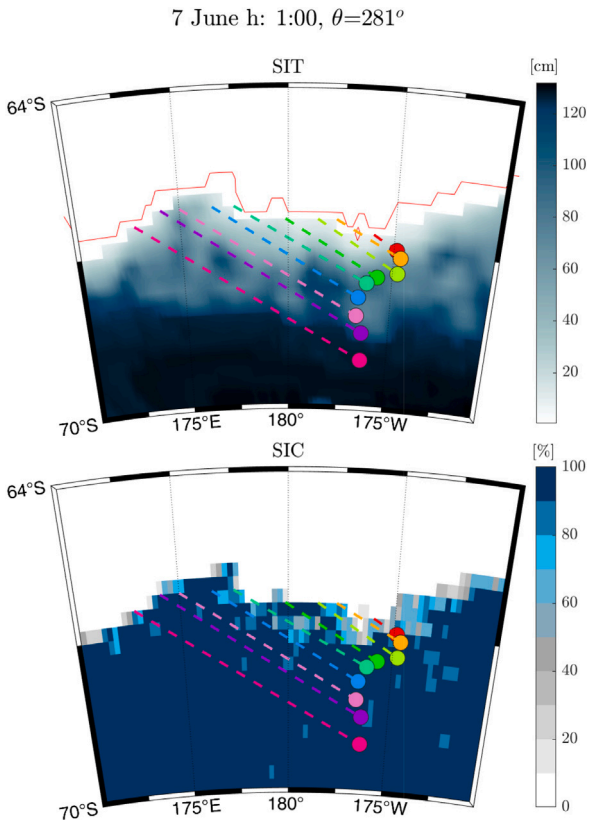

Fig. 1. Sea ice thickness (top) and sea ice concentration (bottom) map for 7 June 2017 at 01:00. Circles indicate the buoy positions, dashed lines the transect travelled by the wave propagating from a mean wave direction $\theta = 281°$ degrees north obtained from ERA5. The red line in the top panel indicates the ice edge using a SIC threshold of 15%.

for the attenuation profiles using $a_n f^n$ type functions results in $n = 4.51 \pm 1.48$ for k_{i_1} and $n = 4.74 \pm 1.46$ for k_{i_2}. In both cases the power law of the CP model is within the uncertainty range.

Considering the whole data set, the difference between h_{CP_1} and h_{CP_2}, which is of course related to the difference between k_{i_1} and k_{i_2}, remains small and tends to zero at high concentrations, see Fig. 3(*a*). However, one would expect the difference between the two attenuations to be greatest when the ocean surface is completely covered by ice. A possible explanation for this counter-intuitive result can be found by looking at the number of available data for each frequency and concentration range, Fig. 3(*b*). In particular, most of the data are available for long waves, i.e. for (old) swell waves, where the equilibrium between the open water source term is reached and the sum $S_{\mathrm{in}} + S_{\mathrm{wc}} + S_{\mathrm{nl}}$ is close to zero (Komen et al., 1996). Therefore, the scaling factor is not relevant in this condition.

On the other hand, data for short waves are limited. For example, at $f = 0.19$ Hz we only have the 20% of the data available at $f = 0.09$ Hz and these are mostly buoys closer to the ice edge with thin ice and low concentration, where wind input is significant. As can be observed in Fig. 3(*a*), in these cases h_{CP_2} can be up to twice the corresponding value h_{CP_1}. However, it is not possible to use these differences to determine which α is the correct one to choose since it would indeed require independent and reliable estimates of ice thickness. Unfortunately, SMOS SIT is known to be significantly underestimated for low values of c (Kaleschke et al., 2024; Paţilea et al., 2019), i.e where the differences between k_{i_1} and k_{i_2} are not negligible.

The CP model calibrated for Arctic conditions (Eq. (3)) can be assessed for the Antarctic winter MIZ by examining the correlation between $h_{\mathrm{CP}_{1,2}}$ and h_{SMOS}. Again, the results should be read as a function of the ice concentration along the transect. As can be seen in Fig. 4 and more quantitatively in Table 1, the correlation increases with c.

Table 1
Linear correlation coefficients between $h_{\mathrm{CP}_{1,2}}$ and h_{SMOS} considering different subsets defined by minimum thresholds of c. For reference, the number of attenuation profiles in each subset is also given. Corr_1 and Corr_2 corresponds to estimates using k_{i_1} and k_{i_2}, respectively.

c [%]	# of data	Corr_1	Corr_2
Any	2006	0.5467	0.5416
≥50	1922	0.6357	0.6313
≥60	1580	0.6529	0.6499
≥70	1100	0.6742	0.6744
≥80	638	0.7363	0.7363
≥90	271	0.8640	0.8626

Eq. (3)'s validity is supported by a correlation coefficient of approximately 0.86 for concentrations above 90%. This range provides greater confidence in both the values of h_{SMOS} and the estimation of $h_{\mathrm{CP}_{1,2}}$, which are independent of the scaling factor for open water source terms. For lower values of c most retrievals indicate $h_{\mathrm{CP}_{1,2}} > h_{\mathrm{SMOS}}$, which is consistent with the known underestimation of h_{SMOS} at lower SIC (Kaleschke et al., 2024).

Finally, it should be noted that to determine sea ice thickness it would be sufficient to know the value of k_i for a single frequency. It is therefore reasonable to ask whether a particular frequency value might be more significant for the calculation of h. Fig. 5(*a*) shows the correlation between the thickness h_{smos} and that obtained by inverting Eq. (3) at each individual frequency. The best correlations for almost any concentration threshold are found for $f = 0.07$ Hz and $f = 0.09$ Hz (waves with a period of 15 s and 10 s respectively). For lower frequencies the correlation is even negative, which may be partly explained by the smaller amount of data available.

Eq. (6) can also be applied for a range of frequencies. In Fig. 5(*b*) we show the effect of including progressively wider frequency ranges that include low swell components. In all cases the correlation is (nearly) saturated for $f < 0.13$ Hz. This result suggests that h can be estimated by following only the swell waves, where the choice of α has little effect.

5. Discussion and concluding remarks

A power law or a combination of power laws, $k_i = A_n f^n$ (Meylan et al., 2014), has often been used as a fitting function when examining the empirical curve fits of observational data for attenuation frequency dependence. Observations in the Arctic and Antarctic marginal ice zones suggested a power coefficient n ranging from 2 to 4 (Meylan et al., 2018; Montiel et al., 2022). However, the knowledge gained – such as agreement or disagreement, coefficients, etc. – tends to be limited to the peculiarities of individual data sets. In this context, from dimensional considerations (Yu et al., 2019) have shown that the discrepancy between these datasets is reduced when normalisation based on ice thickness is applied. In particular, they conclude that the dispersion relation should be of the form

$$k_i = A_n h^{\frac{n}{2}-1} f^n \tag{7}$$

and empirically determined $n = 4.5$ (Yu et al., 2022) from the PIPERS' and other datasets. The physically based CP model has an explicit dependency on sea ice thickness and satisfies Eq. (7) with $n = 5$, i.e. a slightly stronger frequency dependence compared to other authors. Whereas in Yu et al. (2022) the thickness is that at the buoy position, we considered the more physical average thickness of the sea ice over the waves travelled to reach the buoy position.

The calibrated CP model has previously been tested under different sea ice conditions: Western Arctic in October–November 2015 (De Santi et al., 2018), Greenland in March 1997 (De Carolis et al., 2021) and

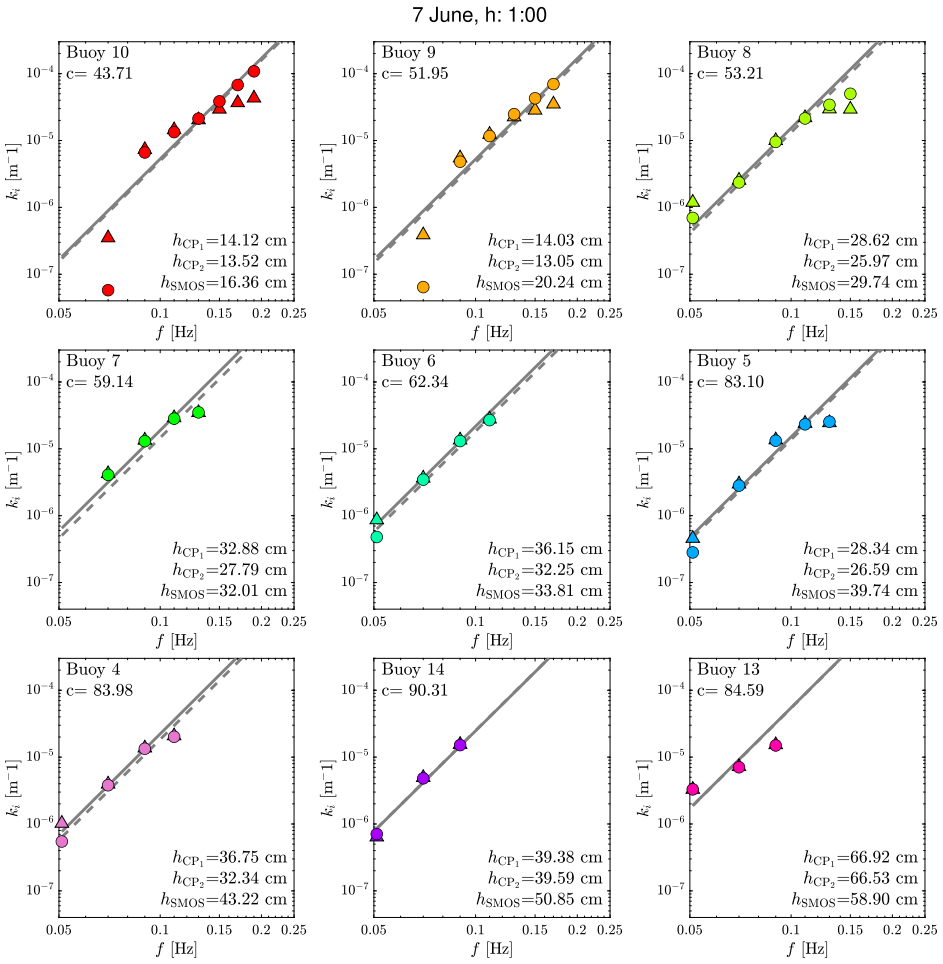

Fig. 2. Hourly mean attenuation profile $k_i(f)$ for each buoy. Triangles indicate k_{i_1}, circles k_{i_2}. Solid lines: CP model attenuation predictions with h_{CP_1}, dashed lines with h_{CP_2}. Data refers to the configuration shown in Fig. 1. The colours of the circles in each panel are the same as those of the corresponding buoy in Fig. 1. The SIC value c, the SIT derived from Eq. (6) and the corresponding predicted attenuation profiles are also given for both rescaling assumptions.

Weddel Sea in April 2000 (De Santi et al., 2018). In addition, an independent non-linear least squares analysis of wave buoy observations from the 2019 SCALE research cruises during the austral winter return $k_i = 8.4\ f^{4.9}$ (Wahlgren et al., 2023), providing good agreement with the CP model and, therefore, further validation of the CP model predictive capabilities. The sources of error in the large scatter obtained when comparing with SMOS SIT and using all valid SIC values in Fig. 4 is more likely attributable to the uncertainties in the satellite retrievals. SMOS-derived thicknesses are underestimated by lower SIC values (Kaleschke et al., 2024), and our results indicate an increase in correlation with increasing SIC, as well as a systematic higher thickness estimated by the CP model. However, o nly a large scale observational campaign of in-situ SIT observations would allow to discriminate the source of uncertainty. Indeed, to fully validate the estimates obtained with the CP model and determine the minimum concentration value at which it remains applicable, an independent and accurate estimate of ice thickness at low sea ice concentrations is necessary.

Further improvements in estimating sea ice thickness depend on the ability to observe and track directional wave spectra. We only considered the mean wave direction, but, in reality, wave energy is directionally spread. A recent study has highlighted that viscous dissipation causes the mean wave direction to gradually shift towards the direction normal to the sea ice edge (Alberello et al., 2024). As the buoys are located up to 600 km from the ice edge, the sea ice transect travelled by the wave should not be straight as assumed in Fig. 1, but may have a curved trajectory. In addition, it should be accounted that ocean waves are often bimodal, with wind and swell waves coexisting but having different mean directions (Alberello et al., 2022; Wahlgren et al., 2023). These issues can only be addressed with measured directional wave spectra, which are not available for the PIPERS dataset.

In this regard, future efforts can leverage on the use of Synthetic Aperture Radar (SAR) satellite acquisition. It is possible to derive the wave direction spectra from SAR sub-images, typically 3–5 km^2 in size (Hasselmann and Hasselmann, 1991). Following the procedure described in De Carolis et al. (2021) and assuming that the spectra are attenuated from one sub-image to the adjacent one according to Eq. (3), it would be possible to estimate the SIT for each sub-image.

It is noteworthy that the majority of the available attenuation data fall within the range of swell waves. This suggests that ice thickness could be estimated from swell tracking alone, which would greatly simplify future work. The measurement of long waves is easier from both buoys, where short waves are usually affected by noise (Thomson et al., 2021), and SAR, which typically have 10–15 m spatial resolution.

In summary, our analysis tested the CP model performances in Antarctic conditions using a coherent set of wave attenuation measurements from the Ross Sea and comparing the resulting SIT with remote sensing estimates. We show that the CP model is in reasonable agreement with wave measurements collected during the PIPERS expedition,

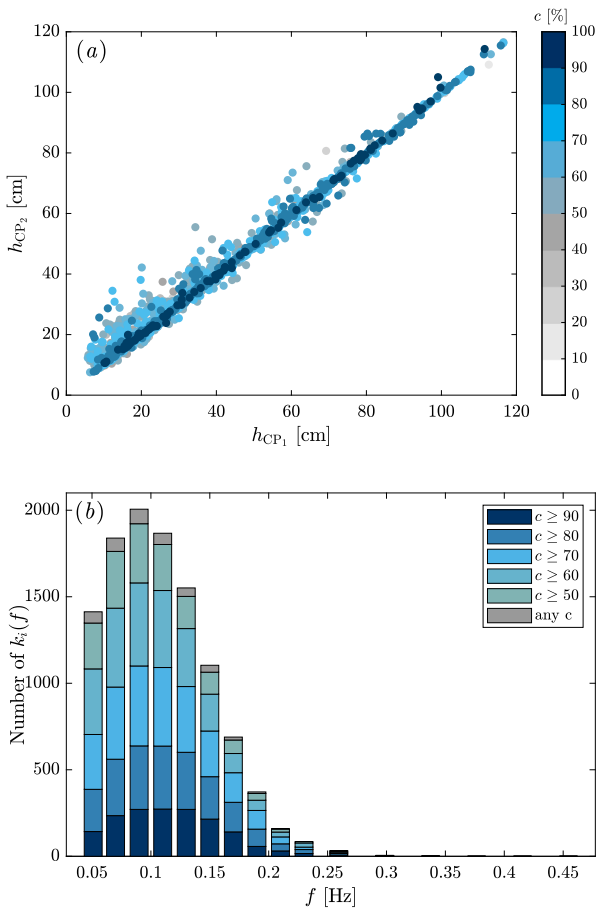

Fig. 3. Top panel: scatter plot between h_{CP_1} and h_{CP_2} with colour scale representing the mean sea ice concentration of the transect c. Bottom panel: Distribution of available data k_i for each frequency and concentration.

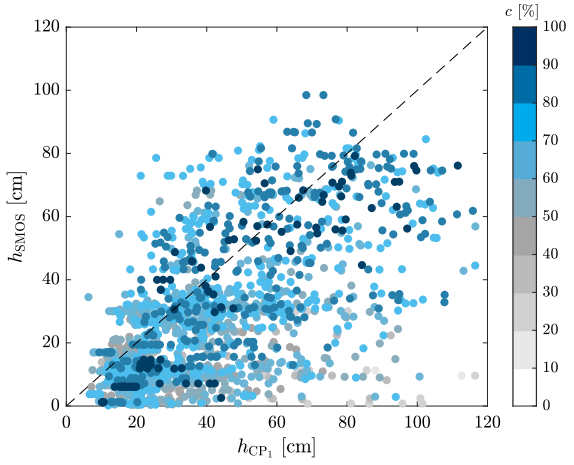

Fig. 4. Scatter plot between h_{CP_1} and h_{SMOS}. The colour scale represents the mean sea ice concentration of the transect c.

both in terms of thickness and frequency dependence, particularly for high concentrations and in the range of swell waves. Overall, the calibrated CP model appears to have a wide applicability and could be implemented in large-scale operational wave models such as WWIII. Moreover, we discussed how the CP has the potential to be used to infer sea ice thickness from SAR images.

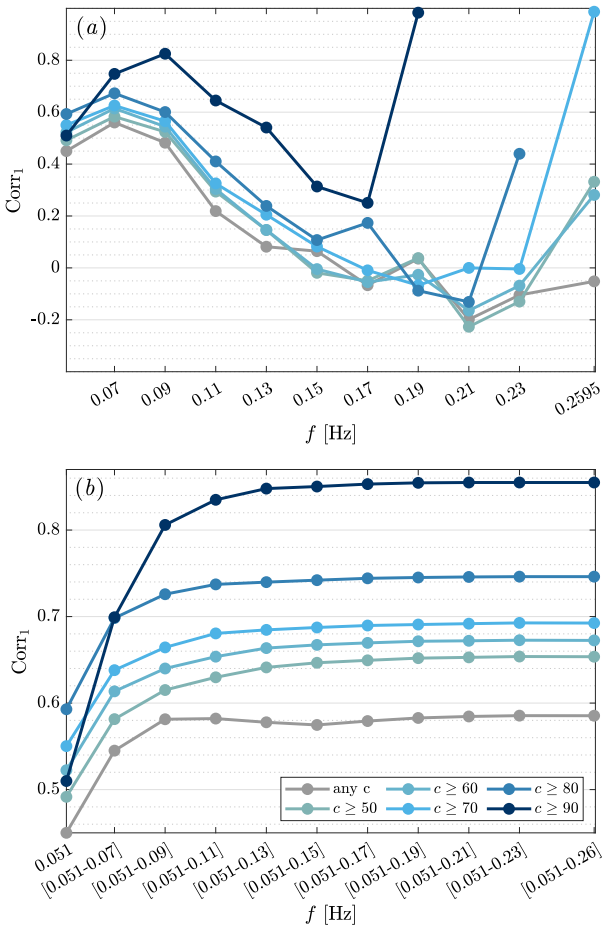

Fig. 5. (*a*) Linear correlation coefficient between h_{smos} and h_{CP_1} obtained by applying Eq. (3) for each frequency separately. (*b*) Linear correlation coefficient between h_{smos} and h_{CP_1} obtained by applying Eq. (6) for incremental subset of frequencies.

CRediT authorship contribution statement

Francesca De Santi: Writing – original draft, Methodology, Conceptualization. **Marcello Vichi:** Writing – review & editing, Methodology. **Alberto Alberello:** Writing – original draft, Methodology.

Declaration of competing interest

The authors declare that they have no known competing financial interests or personal relationships that could have appeared to influence the work reported in this paper.

Data availability

Attenuation profiles are available via https://data.mendeley.com/datasets/5b742jv7t5/1. SIC can be downloaded from https://doi.org/10.1594/PANGAEA.898400 and SIT from https://doi.org/10.1594/PANGAEA.934732. Mean wave direction are taken from https://cds.climate.copernicus.eu/cdsapp#!/dataset/reanalysis-era5-single-levels.

Acknowledgements

AA acknowledges support from EPSRC (EP/Y02012X/1). AA and FDS acknowledge funding from the London Mathematical Society Scheme 4 (Ref. 42250). MV has received funding from the European Union's Horizon 2020 Research and Innovation programme under grant agreement no. 101003826 via project CRiceS (Climate Relevant

interactions and feedbacks: the key role of sea ice and Snow in the polar and global climate system).

References

Alberello, A., Bennetts, L.G., Onorato, M., Vichi, M., MacHutchon, K., Eayrs, C., Ntamba, B.N., Benetazzo, A., Bergamasco, F., Nelli, F., et al., 2022. Three-dimensional imaging of waves and floes in the marginal ice zone during a cyclone. Nature Commun. 13 (1), 4590.

Alberello, A., Onorato, M., Bennetts, L., Vichi, M., Eayrs, C., MacHutchon, K., Toffoli, A., 2019. Brief communication: Pancake ice floe size distribution during the winter expansion of the Antarctic marginal ice zone. Cryosphere 13 (1), 41–48.

Alberello, A., Părău, E.I., Liu, Q., De Santi, F., 2024. Evolution of wave directional properties in sea ice. Ocean Model. 188, 102305.

Ardhuin, F., Rogers, E., Babanin, A.V., Filipot, J.-F., Magne, R., Roland, A., Van Der Westhuysen, A., Queffeulou, P., Lefevre, J.-M., Aouf, L., et al., 2010. Semiempirical dissipation source functions for ocean waves. Part I: Definition, calibration, and validation. J. Phys. Oceanogr. 40 (9), 1917–1941.

Bennetts, L.G., Bitz, C.M., Feltham, D.L., Kohout, A.L., Meylan, M.H., 2022. Theory, modelling and observations of marginal ice zone dynamics: multidisciplinary perspectives and outlooks.

Boutin, G., Lique, C., Ardhuin, F., Rousset, C., Talandier, C., Accensi, M., Girard-Ardhuin, F., 2020. Towards a coupled model to investigate wave–sea ice interactions in the Arctic marginal ice zone. Cryosphere 14 (2), 709–735.

Collins, C., Doble, M., Lund, B., Smith, M., 2018. Observations of surface wave dispersion in the marginal ice zone. J. Geophys. Res.: Oceans 123 (5), 3336–3354.

Day, N., Bennetts, L.G., O'Farrell, S.P., Alberello, A., Montiel, F., 2023. Unsupervised classification of the Antarctic marginal ice zone. Authorea Preprints.

De Carolis, G., Olla, P., De Santi, F., 2021. SAR image wave spectra to retrieve the thickness of grease-pancake sea ice using viscous wave propagation models. Sci. Rep. 11 (1), 1–14.

De Santi, F., De Carolis, G., Olla, P., Doble, M., Cheng, S., Shen, H.H., Wadhams, P., Thomson, J., 2018. On the ocean wave attenuation rate in Grease-Pancake Ice, a comparison of viscous layer propagation models with field data. J. Geophys. Res.: Oceans 123 (8), 5933–5948.

De Santi, F., Olla, P., 2017. Effect of small floating disks on the propagation of gravity waves. Fluid Dyn. Res. 49 (2), 025512.

Doble, M.J., Bidlot, J.-R., 2013. Wave buoy measurements at the antarctic sea ice edge compared with an enhanced ECMWF WAM: Progress towards global waves-in-ice modelling. Ocean Model. 70, 166–173.

Doble, M.J., De Carolis, G., Meylan, M.H., Bidlot, J.-R., Wadhams, P., 2015. Relating wave attenuation to pancake ice thickness, using field measurements and model results. Geophys. Res. Lett. 42 (11), 4473–4481.

Emmanuel, G.V., Rutgersson, A., Wu, L., 2022. Role of source terms in parameterizing wave decay in the marginal ice zones. Ocean Model. 180, 102125.

Gebhardt, C., Bidlot, J.-R., Gemmrich, J., Lehner, S., Pleskachevsky, A., Rosenthal, W., 2016. Wave observation in the marginal ice zone with the TerraSAR-X satellite. Ocean Dyn. 66, 839–852.

Hasselmann, S., Hasselmann, K., 1985. Computations and parameterizations of the nonlinear energy transfer in a gravity-wave spectrum. Part I: A new method for efficient computations of the exact nonlinear transfer integral. J. Phys. Oceanogr. 15 (11), 1369–1377.

Hasselmann, K., Hasselmann, S., 1991. On the nonlinear mapping of an ocean wave spectrum into a synthetic aperture radar image spectrum and its inversion. J. Geophys. Res.: Oceans 96 (C6), 10713–10729.

Herman, A., From apparent attenuation towards physics-based source terms-a perspective on spectral wave modeling in ice-covered seas. Front. Mar. Sci. 11, 1413116.

Herman, A., 2021. Spectral wave energy dissipation due to under-ice turbulence. J. Phys. Oceanogr. 51 (4), 1177–1186.

Hersbach, H., Bell, B., Berrisford, P., Biavati, G., Horányi, A., Muñoz Sabater, J., Nicolas, J., Peubey, C., Radu, R., Rozum, I., Schepers, D., Simmons, A., Soci, C., Dee, D., Thépaut, J.-N., 2023. ERA5 Hourly Data on Single Levels from 1940 to Present. Copernicus Climate Change Service (C3S) Climate Data Store (CDS), http://dx.doi.org/10.24381/cds.adbb2d47.

Iovino, D., Selivanova, J., Masina, S., Cipollone, A., 2022. The antarctic marginal ice zone and Pack Ice Area in CMEMS GREP ensemble reanalysis product. Front. Earth Sci. 10, 745274.

Kaleschke, L., Tian-Kunze, X., Hendricks, S., Ricker, R., 2024. SMOS-derived Antarctic thin sea ice thickness: data description and validation in the Weddell Sea. Earth Syst. Sci. Data 16 (7), 3149–3170.

Keller, J.B., 1998. Gravity waves on ice-covered water. J. Geophys. Res.: Oceans 103 (C4), 7663–7669.

Keller, J.B., Weitz, M., 1953. Reflection and transmission coefficients for waves entering or leaving an icefield. Comm. Pure Appl. Math. 6 (3), 415–417.

Kohout, A.L., Smith, M., Roach, L.A., Williams, G., Montiel, F., Williams, M.J., 2020. Observations of exponential wave attenuation in Antarctic sea ice during the PIPERS campaign. Ann. Glaciol. 61 (82), 196–209.

Komen, G.J., Cavaleri, L., Donelan, M., Hasselmann, K., Hasselmann, S., Janssen, P., 1996. Dynamics and modelling of ocean waves.

Kurtz, N.T., Markus, T., 2012. Satellite observations of antarctic sea ice thickness and volume. J. Geophys. Res.: Oceans 117 (C8).

Marquart, R., Bogaers, A., Skatulla, S., Alberello, A., Toffoli, A., Schwarz, C., Vichi, M., 2021. A computational fluid dynamics model for the small-scale dynamics of wave, ice floe and interstitial grease ice interaction. Fluids 6 (5), 176.

Mei, M., Maksym, T., Weissling, B., Singh, H., 2019. Estimating early-winter antarctic sea ice thickness from deformed ice morphology. Cryosphere.

Melsheimer, C., Spreen, G., 2019. AMSR2 ASI sea ice concentration data, Antarctic, version 5.4 (NetCDF) (July 2012 - December 2019). http://dx.doi.org/10.1594/PANGAEA.898400.

Meylan, M.H., Bennetts, L.G., Kohout, A.L., 2014. In situ measurements and analysis of ocean waves in the Antarctic marginal ice zone. Geophys. Res. Lett. 41 (14), 5046–5051.

Meylan, M.H., Bennetts, L.G., Mosig, J., Rogers, W., Doble, M., Peter, M.A., 2018. Dispersion relations, power laws, and energy loss for waves in the marginal ice zone. J. Geophys. Res.: Oceans 123 (5), 3322–3335.

Montiel, F., Kohout, A.L., Roach, L.A., 2022. Physical drivers of ocean wave attenuation in the marginal ice zone. J. Phys. Oceanogr. 52 (5), 889–906.

Olla, P., De Carolis, G., De Santi, F., 2021. Diffusion of gravity waves by random space inhomogeneities in pancake-ice fields. Theory and validation with wave buoys and synthetic aperture radar. Phys. Fluids 33 (9), 096601.

Paţilea, C., Heygster, G., Huntemann, M., Spreen, G., 2019. Combined SMAP–SMOS thin sea ice thickness retrieval. Cryosphere 13 (2), 675–691.

Pedersen, L.T., Coon, M.D., 2004. A sea ice model for the marginal ice zone with an application to the greenland sea. J. Geophys. Res.: Oceans 109 (C3).

Rogers, E., 2020. Dissipation profiles for PIPERS dataset. http://dx.doi.org/10.17632/5b742jv7t5.1, URL https://data.mendeley.com/datasets/5b742jv7t5/1.

Rogers, W.E., Meylan, M.H., Kohout, A.L., 2021. Estimates of spectral wave attenuation in Antarctic sea ice, using model/data inversion. Cold Reg. Sci. & Technol. 182, 103198.

Rogers, W.E., Orzech, M.D., 2013. Implementation and Testing of Ice and Mud Source Functions in WAVEWATCH Iii (Registered Trademark). Technical Report NRL/MR/7320–13-9462, Naval Research Lab Stennis Detachment Stennis Space Center MS Oceanography Div, Office of Naval Research, One Liberty Center, Arlington, Va.

Shen, H., Perrie, W., Hu, Y., He, Y., 2018. Remote sensing of waves propagating in the marginal ice zone by SAR. J. Geophys. Res.: Oceans 123 (1), 189–200.

Squire, V.A., 2020. Ocean wave interactions with sea ice: A reappraisal. Annu. Rev. Fluid Mech. 52, 37–60.

Squire, V., 2022. Marginal ice zone dynamics. Philos. Trans. Ser. A Math. Phys. Eng. Sci. 380.

Thomson, J., 2022. Wave propagation in the marginal ice zone: connections and feedback mechanisms within the air–ice–ocean system. Phil. Trans. R. Soc. A 380 (2235), 20210251.

Thomson, J., Ackley, S., Girard-Ardhuin, F., Ardhuin, F., Babanin, A., Boutin, G., Brozena, J., Cheng, S., Collins, C., Doble, M., et al., 2018. Overview of the arctic sea state and boundary layer physics program. J. Geophys. Res.: Oceans 123 (12), 8674–8687.

Thomson, J., Hošeková, L., Meylan, M.H., Kohout, A.L., Kumar, N., 2021. Spurious rollover of wave attenuation rates in sea ice caused by noise in field measurements. J. Geophys. Res.: Oceans 126 (3), e2020JC016606.

Tian-Kunze, X., Kaleschke, L., 2021. SMOS-derived sea ice thickness in the Antarctic from 2010 to 2020. http://dx.doi.org/10.1594/PANGAEA.934732.

Tolman, H.L., et al., 2009. User Manual and System Documentation of WAVEWATCH III TM Version 3.14. Technical Note, MMAB Contribution 276.

Vichi, M., 2022. An indicator of sea ice variability for the Antarctic marginal ice zone. Cryosphere 16 (10), 4087–4106.

Vichi, M., Eayrs, C., Alberello, A., Bekker, A., Bennetts, L., Holland, D., de Jong, E., Joubert, W., MacHutchon, K., Messori, G., et al., 2019. Effects of an explosive polar cyclone crossing the Antarctic marginal ice zone. Geophys. Res. Lett. 46 (11), 5948–5958.

Wadhams, P., Lange, M.A., Ackley, S.F., 1987. The ice thickness distribution across the Atlantic Sector of the Antarctic Ocean in midwinter. J. Geophys. Res.: Oceans (ISSN: 2156-2202) 92 (C13), 14535–14552.

Wadhams, P., Parmiggiani, F.F., de Carolis, G., Desiderio, D., Doble, M.J., 2004. SAR imaging of wave dispersion in Antarctic pancake ice and its use in measuring ice thickness. Geophys. Res. Lett. 31 (15).

Wadhams, P., Squire, V.A., Goodman, D.J., Cowan, A.M., Moore, S.C., 1988. The attenuation rates of ocean waves in the marginal ice zone. J. Geophys. Res.: Oceans 93 (C6), 6799–6818.

Wahlgren, S., Thomson, J., Biddle, L.C., Swart, S., 2023. Direct observations of wave-sea ice interactions in the Antarctic marginal ice zone. J. Geophys. Res.: Oceans 128 (10), e2023JC019948.

Williams, G., Maksym, T., Wilkinson, J., Kunz, C., Murphy, C., Kimball, P., Singh, H., 2015. Thick and deformed antarctic sea ice mapped with autonomous underwater vehicles. Nat. Geosci. 8, 61–67.

Williams, T.D., Rampal, P., Bouillon, S., 2017. Wave–ice interactions in the neXtSIM sea-ice model. Cryosphere 11 (5), 2117–2135.

Yu, J., Rogers, W.E., Wang, D.W., 2019. A scaling for wave dispersion relationships in ice-covered waters. J. Geophys. Res.: Oceans 124 (11), 8429–8438.

Yu, J., Rogers, W.E., Wang, D.W., 2022. A new method for parameterization of wave dissipation by sea ice. Cold Reg. Sci. & Technol. 199, 103582.